Simulation Model of Common-Mode Chokes for High-Power Applications

A. Muetze
C. R. Sullivan

Found in *IEEE Industry Applications Society Annual Meeting,* Sept. 2007, pp. 1810–1815.

Simulation Model of Common-Mode Chokes for High-Power Applications

Charles R. Sullivan
Thayer School of Engineering
Dartmouth College, Hanover, NH 03755 USA
chrs@dartmouth.edu

Annette Muetze
School of Engineering
University of Warwick, CV4 7AL, UK
a.muetze@warwick.ac.uk

***Abstract*— Linear and nonlinear Cauer-network models for nanocrystalline inductor cores are developed and used for circuit simulations of common-mode chokes for inverter-based drive systems of several hundred kW. Experimental measurements of the chokes' performance in a high-power test bed are compared to the model results. When the model is based on measured characteristics of the material used, the match to measured behavior is good. Damping inherent in the material characteristic is adequate, such that additional damping is not useful. The primary limitation to accurate prediction of loss in practice is the tolerance on specifications of core characteristics, particularly at high frequency where limits are not specified.**

I. Introduction

In inverter-based drive systems, high-frequency common-mode voltages at the inverter output can lead to high-frequency common-mode currents. Depending on the overall system, notably the drive size and presence of additional mitigation techniques, early drive failure can result from bearing currents that arise from several different mechanisms [1]–[7]. These effects are increasingly important with increasing machine size. Other phenomena include wide-band electromagnetic interference and interference with ground fault protection systems in industrial facilities. Common-mode chokes that are placed in the inverter-output (Fig. 1) can be a cost-effective method of reducing such ground currents [4], [6].

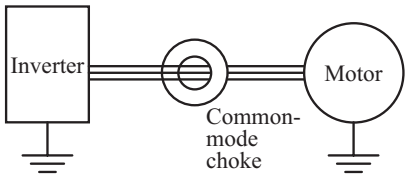

Fig. 1. Simplified sketch to illustrate placement of common-mode choke in the inverter-output.

Because of the large magnitudes of both the high-frequency ground-current and the phase currents, where the latter leads to motor leads with large diameters, the requirements for such chokes differ from standard choke design. Notably, use of several single-turn feed-through chokes in series is likely to be a more practical choice than wound chokes, [8] (Fig. 2).

Core materials for common-mode chokes in this application should preferably have both high saturation flux density and high permeability [8]. Amorphous and nanocrystalline materials have good properties in both these aspects. However, in the frequency range of hundreds of kHz (typical of the ring frequency between the common-mode choke inductance and the motor capacitance), their permeability is dropping off with frequency. While the permeability is still large enough to be advantageous for the application, the frequency dependence complicates the modeling; the input signal to the filter network is a rapid step that contain energy in a wide spectrum of frequencies. In this paper, we develop improved linear and nonlinear simulation models for nanocrystalline cores, and compare the results to experimental measurements. We also examine the effect of added damping on the simulated behavior.

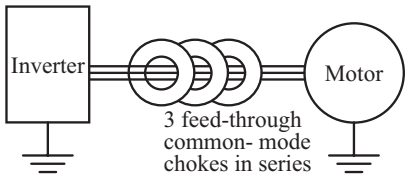

Fig. 2. Simplified sketch to illustrate use of several single-turn feed-through common-mode choke in series instead of wound chokes.

For the purpose of studying common-mode behavior, the machine-inverter configuration is modeled by a per-phase RLC network, similar to what is done in [4], [5]. Each switching transition is analyzed independently, which can be justified by the fact that the transient is short compared to the typical time between switching transitions. With effectively used common-mode chokes, the ring period is long compared to the transition time, and the details of the switching transition waveform become unimportant; the system can be treated as a step input to the RLC network [8].

We first explain the simulation technique and development of the model (Section II), summarize the experimental measurements of the permeability (Section III) which are used as input to the model, and experimental measurements of common-mode currents (Section IV), which are used for comparison to the simulation results. Then, the simulation results and the ability and limits of the modeling approach are discussed (Section V). At the end, conclusions are drawn (Section VI).

II. Simulation Technique

A. Preliminary choices

Transient simulations were conducted using both the SIMPLIS circuit simulator [9] and using numerical solutions to the ordinary differential equations that describe the circuit

0197-2618/07/$25.00 © 2007 IEEE

using the "ode23" solver in MATLAB [10]. After initial simulations modeling a full three-phase system with a common-mode inductor confirmed that the ground-current behavior was identical to that of a single-phase model using the average phase voltage, simulations used a single-phase model.

Since the core permeability is not constant in the frequency range of interest, models with frequency-dependent permeability were developed using a Cauer network [8], [11], to allow a more accurate simulation. As suggested in [8], a Cauer 1 network (with series inductors and shunt resistors) was used in place of the Cauer 2 network (with shunt inductors and series resistors). This allows including saturation in each portion of the core in a more physically realistic manner than is possible in a Cauer 2 network [12].

B. Parameter tuning

The element values in the network were tuned to match the model's frequency-dependent permeability to published or measured core characteristics, using a two-stage process and a numerical optimization code implemented in MATLAB: First, approximate values were found by assuming that both the resistor values and the inductor values in the network were logarithmically spaced, such that the optimization could operate on just four variables: the inductances and resistances of the first and last stages of the network. The optimization used the MATLAB implementation of the Nelder-Mead simplex algorithm [13] to minimize the sum of the square of the percentage error in complex impedance at each frequency point. The set of values found this way was then used as the starting point for an optimization using the same algorithm to fine tune all the individual resistor and inductor values. Through testing this two-step optimization process for different numbers of elements in the network, we found that a fifth-order network was adequate to give an excellent match to the permeability characteristic, with less than 0.139% average error. (Error for a forth-order network was slightly higher at 0.153% average error, whereas sixth- or seventh-order networks did not noticeably decrease error, still having 0.139% average error.)

C. Permeability measurements

Our initial model was based on a model fitted to permeability data for a similar nanocrystalline material plotted in [14], but the results of simulations using this model did not match our experimental measurements very closely, so we performed our own permeability measurements using an Agilent 4294A impedance analyzer with a single-turn winding. In this paragraph we only anticipate the results so as to continue with the discussion of the simulation technique. The measurements will be described more in detail further below (Section III-A). Fig. 3 shows the measured complex permeability along with the permeability extracted from the impedance of the Cauer-network model. The complex relative permeability, $\underline{\mu}_{\mathrm{r}}^{*}$, was calculated from the Cauer-network model as

$$\underline{\mu}_{\mathrm{r}}^{*} = \frac{\underline{Z}_{\mathrm{sim}}\ell_{\mathrm{c}}}{j\omega\mu_0 A_{\mathrm{c}}} \tag{1}$$

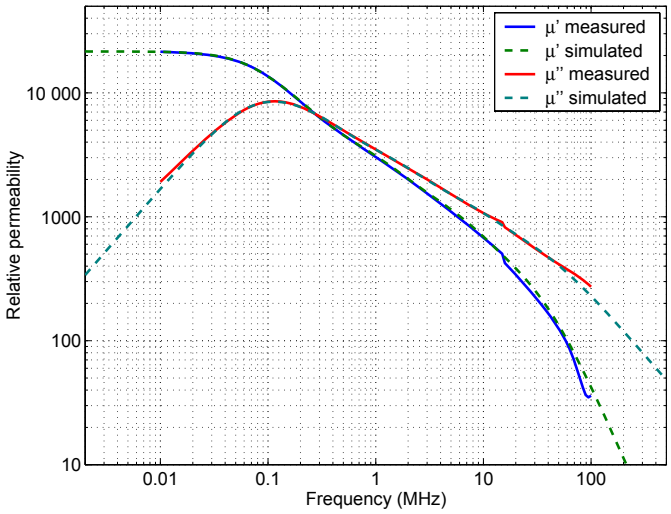

Fig. 3. Measured permeability and permeability calculated from the impedance of the Cauer-network model; measurements used an Agilent 4294A impedance analyzer with a single-turn winding, providing a small-signal measurement in which the cores under test do not exhibit saturation. Plotted are the real (μ') and imaginary (μ'') parts of complex relative permeability $\underline{\mu}_{\mathrm{r}}^{*} = \mu' - j\mu''$.

where $\underline{Z}_{\mathrm{sim}}$, is the impedance of the Cauer-network model, ℓ_{c} and A_{c} are the magnetic path length and cross-sectional area of the core, ω is the radian measurement frequency, and μ_0 is the permeability of free space.

D. Linear circuit (circuit simulator)

The simulation model circuit using the SIMPLIS [9] circuit simulator is shown in Fig. 4. In addition to the Cauer network, it includes an ideal transformer implemented with a voltage-controlled voltage source and a current-controlled current source, used to scale the material model to the core size and number of turns. The capacitor C1 represents the total effective capacitance through which the high-frequency common-mode current flows.

E. Non-linear circuit (MATLAB)

Subsequent simulations were implemented with a MATLAB numerical differential-equation solution, based on the same topology, but with nonlinear inductors. Furthermore, an additional series inductance was included, representing wiring inductance. For the test setup used in the work presented here (Section IV) the value of this inductance had been identified to be 739 nH [15].

The nonlinear inductor characteristics were modeled using a dual-slope function [16]

$$i = \frac{s_1 - s_2}{\left(b^{-n} + \lambda^{-n}\right)^{\frac{1}{n}}} + s_2\lambda \ , \tag{2}$$

where λ is the flux linkage, i is the winding current, and b, n, s_1, and s_2 are parameters chosen by hand to match the curve to a measured B-H loop: s_1 is the slope at low flux levels, s_2 the saturated slope, b the saturation breakpoint, and n is used to determine the sharpness of the transition.

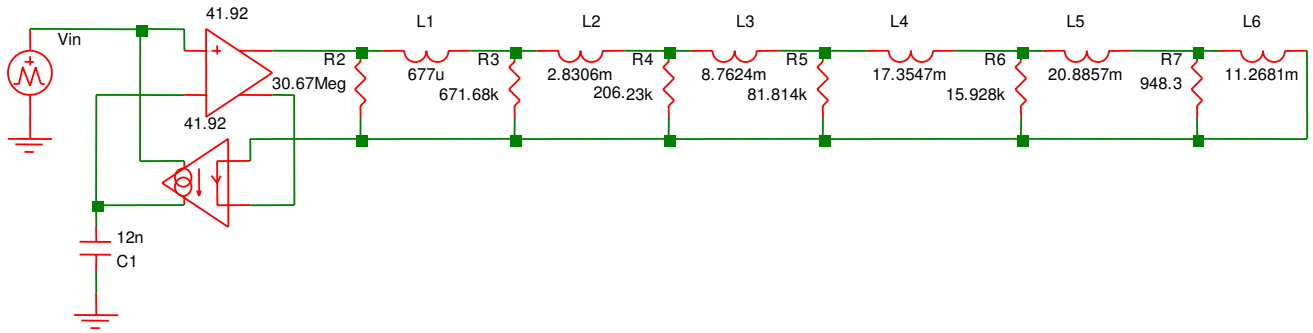

Fig. 4. Simulation model including a Cauer 1 network to capture the effect of frequency-dependent core material. In this schematic, a linear model is shown; in the nonlinear model each inductor is nonlinear, with saturation occurring at the same current (Section II-E). The capacitance is adjusted for simulations of different configurations of the experimental test setup (Section IV).

The B-H loop measurement used for fitting this curve is described below (Section III-B). The values were matched for the B-H loop measured at 100 Hz. The values used were $s_1 = 6.659 \times 10^4$ H^{-1}; $s_2 = 4 \times 10^7$ H^{-1}; $b = 121.43$ μWb; and $n = 35$. Since these measurement were based on a specific core, the values were then scaled according to core area and length for other core sizes, and for individual inductors within the Cauer model.

III. Permeability Measurements

A. Frequency dependence (linear B-H, small signals)

A set of small-signal measurements was carried out using six commercially available cores, M1 through M6 (Table I), and an Agilent 4294A impedance analyzer with a single-turn winding. All cores were analyzed over a frequency range 100 kHz through to 10 MHz.

TABLE I
PARAMETERS OF COMMON-MODE CHOKES USED

Choke label	Tabulated inductance* [μH]	Outer diameter [mm]	Window diameter [mm]	Length [mm]
M1, M2	24.1...48.2	80	63	30
M3	23.3...46.6	63	50	30
M4, M5	13.2...29.7	63	50	20
M6	22.5...45.0	108	70	36

*) : A_L-value at 10 kHz.

For each measurement frequency, the complex relative permeability $\underline{\mu}_r^*$ was calculated as

$$\underline{\mu}_r^* = \frac{\underline{Z}_{meas}\ell_c}{j\omega\mu_0 A_c} \quad , \tag{3}$$

similar to (1), where $\underline{Z}_{meas}$ is the measured complex impedance. Except for one, all our samples had very closely matched high-frequency and low-frequency permeability. The cores had all been obtained at once and we assume these five were all from the same batch. The results have already been shown above (Fig. 3) (which exclude the values of the one sample with slightly different behavior).

B. B-H loop (non-linear B-H, large signals)

A series of B-H loop measurements was carried out on the M4 core using the two-winding method: One winding was driven from a power amplifier (Halfer P7000) with a sinusoidal voltage, with a current measurement used to obtain the magnetic field H. A second open-circuited winding with a voltage measurement was used to obtain the magnetic field density B through integration performed in software post-processing. The measurements were carried out at 100 Hz, 1 kHz, 10 kHz, 100 kHz, and 300 kHz for currents up to 14 A (300 kHz: 5 A). Exemplarily, the results for 5 A are shown in Fig. 5. These results clearly illustrate the saturation of the material at low frequencies (100 Hz, 1 kHz) and the almost linear behavior due to relative permeability decreasing with increasing frequency at higher frequencies (100 kHz, 300 kHz).

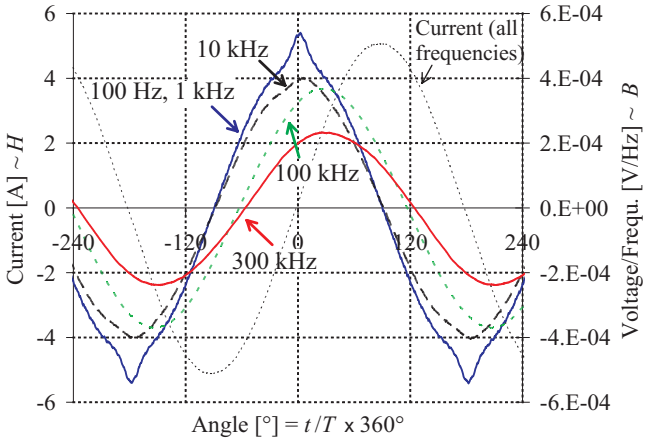

Fig. 5. Measured voltages at 5 A current and different frequencies using the two-winding method and a power amplifier with a sinusoidal voltage; core M4. The effect of the relative permeability decreasing with increasing frequency is clearly to see from the decreasing degree of saturation with increasing frequency.

IV. Measurement of Common-Mode Currents

The results of the simulations are compared to experimental results that have been presented in a previous publication with a related but different focus [15]. In [15], a series of tests has been reported to show the feasibility of a low-cost method for experimental investigation of such common-mode chokes of inverter-based drive systems of several hundred kW. In this paper, we only review what is relevant for the experimental results we are using for verification of the proposed simulation technique:

A. Test setup

The test setup consists of a 4 kW 230 V IGBT-inverter, a 11 kW squirrel-cage induction motor, and one very short #6 stranded wire motor-inverter interconnect of only 25 cm length. Only one motor terminal and one inverter-leg were connected. The cable was kept at minimum length to limit its influence on the ground-current generation. Without any additional devices, the measured peak high-frequency ground current was $I_{\mathrm{p}} = 11.9$ A, which is a typical value for a drive of this rating. This amplitude was increased artificially by more than 500% as follows: Drawing from the understanding that off-the shelf machines show mainly capacitive behavior at the high frequencies of the common-mode current, additional high AC voltage polypropylene foil capacitors were connected between the phase terminal connection and the protective earth of the drive (Fig. 6(a)). For the different values of additional capacitors C_{a} (including $C_{\mathrm{a}} = 0$), commercially available feed-through common-mode chokes were placed between the inverter and the motor. These chokes were obtained from the cores listed above (Table I). Both individual cores and combinations of cores were investigated. If connected, the additional capacitors were on the motor side of the choke (Fig. 6(b)).

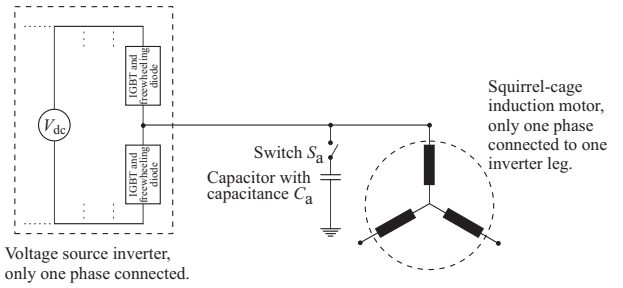

(a) Without common-mode choke(s).

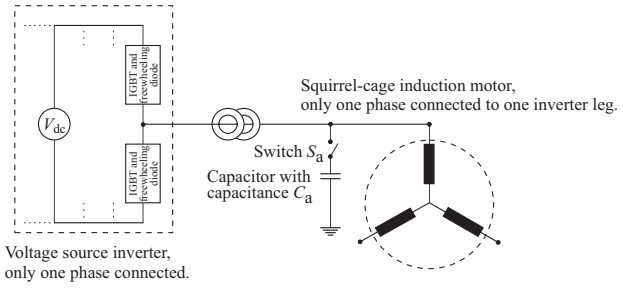

(b) With common-mode choke(s).

Fig. 6. Test setup for measurement of common-mode currents with and without common-mode chokes: one motor terminal connected to one inverter leg and additional capacitors with capacitance C_{a} connected at the motor terminal [15].

B. Measured common-mode currents

With increasing value of C_{a}, the peak current amplitude increases, reaching $I_{\mathrm{p,30nF}} = 63.1$ A $= 5.3 \cdot I_{\mathrm{p,0nF}}$ at $C_{\mathrm{a}} = 30$ nF (Figs. 7 and 8), where $I_{\mathrm{p,0nF}}$ is the peak current amplitude with no additional capacitors nor common-mode chokes. Both with and without chokes, the peak ground current amplitude increases approximately linear with increasing values of C_{a}.

From the different measurements taken, the results for M1 and M3 are also shown exemplarily in Fig. 7, clearly illustrating the effectiveness of the chokes to reduce the common-mode current. Furthermore, Figs. 8 and 9 illustrate how the comparatively large value of the choke inductance significantly reduces the ringing of the ground current by approximately one order of magnitude. For further discussion of these results, we refer to [15].

V. Simulation Results

A. Input voltage

As shown in [8], the detailed shape of the input voltage step makes little difference to the current waveform in designs chosen to effectively attenuate common-mode currents and avoid saturation. However, the tests we performed included designs in which there was significant saturation, and designs in which the choke as small enough that the ring periods that were not long compared to the rise time. Thus the waveform could matter for some simulations. Based on a measurement of the inverter leg with no load, we approximated the input waveform as a linear ramp from the negative rail to zero in 67 ns and a linear ramp from zero to the positive rail in 150 ns. The actual waveform varies between switching instances and may also be affected by the choke and capacitor configuration, and thus using this single waveform to represent all of the cases simulated may have introduced a non-negligible factor of uncertainty.

B. Not saturated vs. saturated cases

The waveforms for two cases are compared in Figs. 10 and 11; these two cases are chosen to illustrate behavior without and with saturation, but with otherwise similar behavior. The match to experimental results is good, but the detailed behavior in saturation shows some differences near the peak. In addition, note that the ringing is damped significantly more rapidly in the experimental measurement with saturation. One possible explanation for this would be if there were significant hysteresis losses not captured by the loss in the Cauer network, which was tuned only to match small-signal loss measurements.

The simulation results for a range of different experimentally measured configurations are compared in Fig. 12, which plots the peak currents observed experimentally vs. those observed in simulations. Three different capacitor values ($C_{\mathrm{a}} =$ 10 nF, 20 nF, and 30 nF, in addition to the effective machine capacitance that was determined to 4.27 nF) are used with three different choke configurations (M1, M3, and M3 & M4), for a total of nine different setups. The match is very good. We attribute the observed error to noise on the current measurements, to discrepancies in the input voltage waveform, and to the limitations of our core model in capturing saturation and hysteresis accurately. Although the order of the Cauer model is sufficient to capture the small-signal behavior very accurately over a wide frequency range, a higher-order model may have advantages in accurately modeling saturation. However, this would come at the price of increased implementation and computational effort. Yet, the

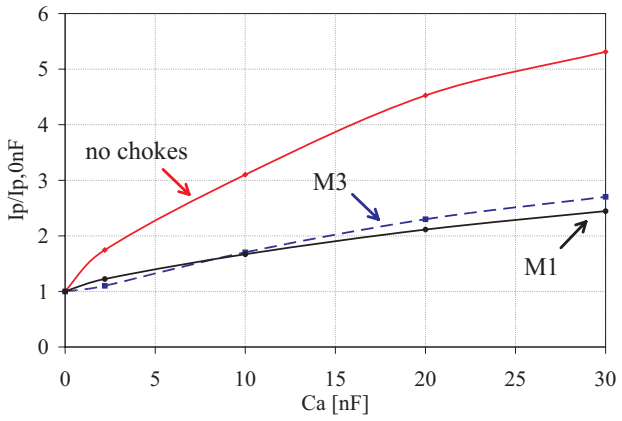

Fig. 7. Measured current increase with additional capacitance C_a without choke and with chokes M1 and M3, $I_{p,0nF}$: peak amplitude with no additional capacitors, I_p: peak current amplitude with additional capacitors with capacitance C_a, [15].

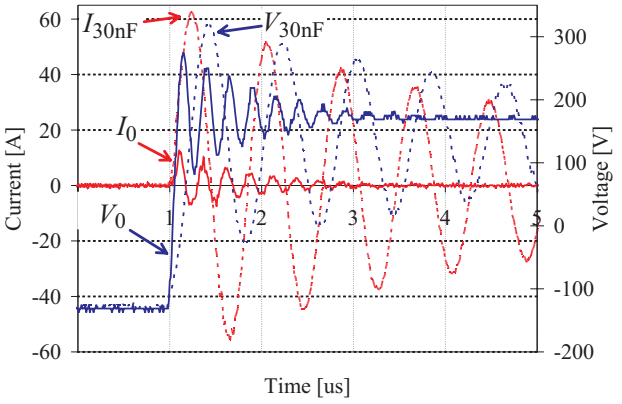

Fig. 8. Measured currents and voltages with $C_a = 0$ nF (I_0, V_0) and $C_a = 30$ nF (I_{30nF}, V_{30nF}), and without common-mode chokes, [15].

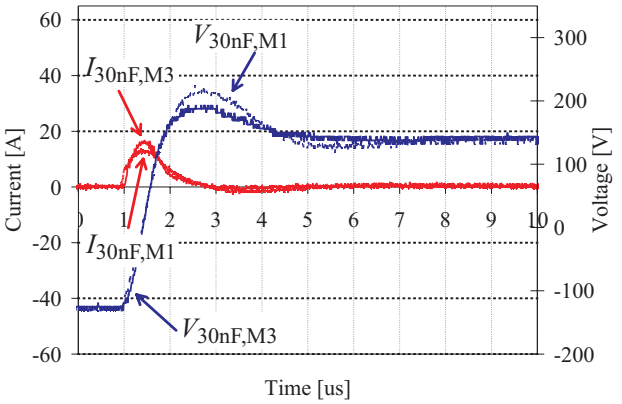

Fig. 9. Measured currents and voltages with $C_a = 30$ nF and chokes M1 ($I_{30nF,M1}$, $V_{30nF,M1}$) and M3 ($I_{30nF,M3}$, $V_{30nF,M3}$), [15].

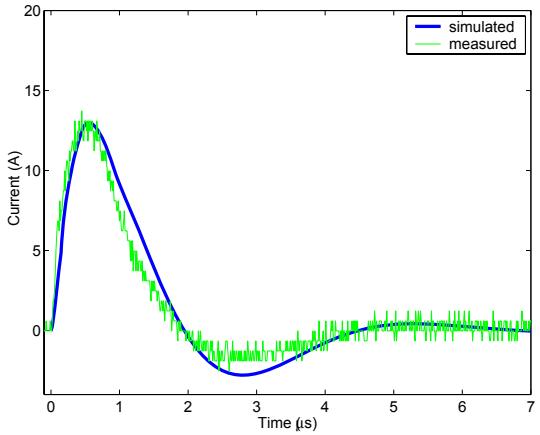

Fig. 10. Comparison of simulated and measured current waveforms with a larger core that does not exhibit significant saturation; additional capacitor C_a = 30 nF, common-mode choke M1.

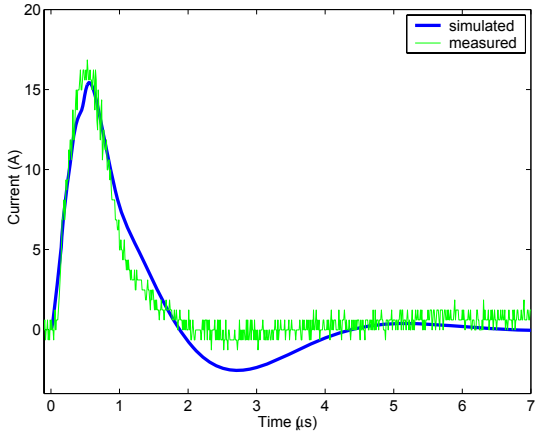

Fig. 11. Comparison of simulated and measured current waveforms with a smaller core that partially saturates; additional capacitor C_a = 30 nF, common-mode choke M3.

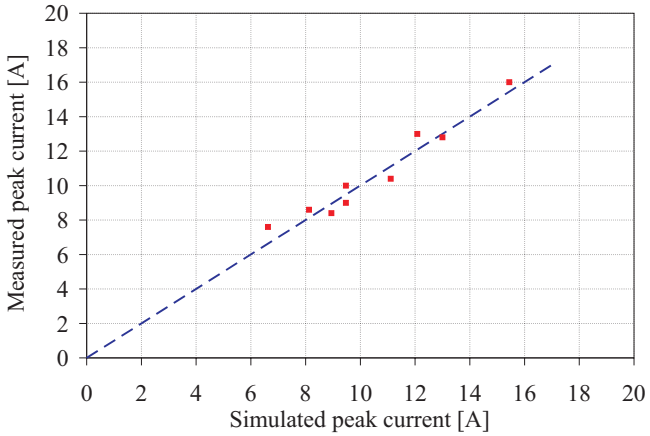

Fig. 12. Comparison of simulated and measured peak currents. The line indicates equal simulated and measured currents; configurations with C_a = 10 nF, 20 nF, and 30 nF, in addition to the machine capacitance and chokes M1, M3, and M3 & M4.

current model is good enough to match the results to within the certainty of the experimental measurements, and is also good enough for practical design work.

C. Practical limits

In practice, the limiting factor on predicting performance from our model is the tolerance on the core manufacturer's permeability specifications, which allow a factor-of-two variation in low-frequency permeability. The tolerance and typical vari-

ability of high-frequency permeability is unknown. Most of the samples we tested had very closely matched high-frequency and low-frequency permeability, and so these measurements do not help us assess the possible variation in high-frequency permeability.

D. Additional damping

Adding damping to an ideal LC system can reduce the peak current as well as reducing the duration of the ringing, as has been proposed for this application [4]. To investigate the possible advantage of adding damping, a series of simulations was conducted with varying resistance in parallel with the Cauer choke model. The simulated choke was based on the first design in Table IV of [8]: based on an approximate peak current limit of 5 A with a capacitance of 12 nF to ground, and a 187-V step, a choke with 1.0 cm^2 core area and 12.3 cm magnetic path length. Results, including both an ideal choke model and the frequency-dependent Cauer model based on the nanocrystalline material behavior plotted in [12], are shown in Fig. 13. With the ideal model, a reduction in peak current is observed, as analyzed in detail in [4]. However, no reduction in the peak current is possible with the frequency-dependent choke model. We explain this by the fact that the nanocrystalline core is lossy at the ring frequency, and the damping that it provides is already sufficient. Adding damping would only be advantageous with a lower loss core material, such as some ferrites. Note that although the scale on the plot in Fig. 13 allows confirming only that any improvement in peak current when a damping resistor is added to the realistic model is insignificant at best, zooming in more closely on the data confirms that as the resistor value is decreased, the peak current monotonically increases for all the values plotted, which shows that the resistor has no benefit in the case examined. We also note that the comparisons in Figs. 10 and 11 show that the damping provided by nanocrystalline cores is greater in practice than is predicted by our model, further confirming that a damping resistor would rarely be useful with a nanocrystalline core.

VI. Conclusions

Comparison of experimental measurements and simulations of CM chokes in for inverter-based drive systems of several hundred kW indicate that an accurate frequency-dependent choke model is important. Cauer-network models can be used to accurately model the frequency-dependent permeability of nanocrystalline materials, and can incorporate saturation characteristics. When the model is based on measured characteristics of the material used, the match to measured behavior is good. Damping inherent in the material characteristic is adequate, such that additional damping is not useful. The primary limitation to accurate prediction of loss in practice is the tolerance on specifications of core characteristics, particularly at high frequency where limits are not specified.

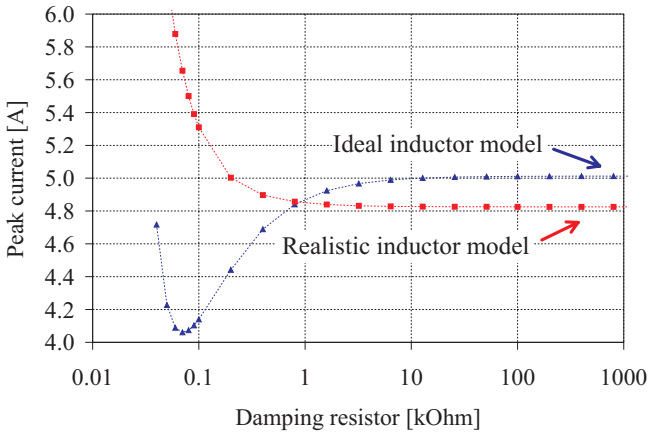

Fig. 13. Simulated peak current with a damping resistor in parallel with the choke. The damping can reduce the peak current when an ideal inductor model is used. However, when a realistic frequency-dependent model of an inductor using a nanocrystalline core material is used, the damping resistor only increases the current.

References

[1] S. Chen, T. Lipo, and D. Novotny, "Circulating type motor bearing current in inverter drives," *in Proceedings 31th IEEE Industry Society Annual Meeting*, vol. 1, pp. 162–167, 1996.

[2] J. Ollila, T. Hammar, J. Lisakkala, and H. Tuusa, "A new reason for bearing current damanges in variable speed drives," *in Proceedings 7th European Conference on Power Electronics and Applications (EPE)*, pp. 2539–2542, Trondheim, 1997.

[3] P. Link, "Minimizing electric bearing currents in ASD systems," *IEEE Industry Applications Magazine*, vol. 5, no. 4, pp. 55–66, 1999.

[4] S. Ogasawara and H. Akagi, "Modeling and damping of high-frequency leakage currents in PWM inverter-fed AC motor drive systems," *IEEE Transactions in Industry Applications*, vol. 32, no. 5, pp. 1105–1114, 1996.

[5] I. Boldea and S. Nasar, *Electric Drives*. CRC Press LLC, Florida, 1999.

[6] C. Mei, J. Balda, W. Waite, and K. Carr, "Minimization and cancellation of common-mode currents, shaft voltages, and bearing currents for induction motor drives," *in Proceedings 34th Power Electronics Specialist Conference (PESC)*, vol. 3, pp. 1127–1132, Cape Girardeau, 2003.

[7] A. Muetze, "Bearing currents in inverter-fed ac motors," Ph.D. dissertation, Darmstadt University of Technology, Shaker Verlag, Aachen, 2004.

[8] A. Muetze and C. R. Sullivan, "Simplified design of common-mode chokes for reduction of motor ground currents in inverter drives," in *Proceedings 41th IEEE Industry Society Annual Meeting*, 2006.

[9] Transim Technology Corporation Portland, Oregon, USA, "SIMPLIS circuit simulator, in Catena SIMetrix/SIMPLIS version 5.3." [Online]. Available: http://www.catena.uk.com/site/products/simplis.htm

[10] L. F. Shampine and M. W. Reichelt, "The MATLAB ODE suite," *SIAM Journal on Scientific Computing*, vol. 18, no. 1, pp. 1–22, 1997.

[11] B. Revol, H. Chazal, and J. Roudet, "Common mode choke characterisation method and modelling for emi filter in power electronics," in *EPE*, 2003.

[12] P. Holmberg, A. Bergqvist, and G. Engdahl, "Modelling eddy currents and hysteresis in a transformer laminate," *IEEE Transactions on Magnetics*, vol. 33, no. 2, 1997.

[13] J. Lagarias, J. Reeds, M. Wright, and P. Wright, "Convergence properties of the Nelder-Mead simplex method in low dimensions," *SIAM Journal on Optimization*, vol. 9, no. 1, pp. 112–47, 1998.

[14] G. Herzer, *Nanocrystalline Soft Magnetic Alloys*. Elsevier Science B.V., 1997, vol. 10, ch. 3.

[15] A. Muetze and B. S. Heng, "Low-cost low-power test-bed for experimental investigation of common-mode chokes for high-power applications," in *Proceedings of the IEEE 5th International Electric Machines and Drives Conference (IEMDC)*, 2007.

[16] C. Sullivan and S. Sanders, "Models for induction machines with magnetic saturation of the main flux path," *IEEE Transactions on Industry Applications*, vol. 31, no. 4, pp. 907–17, 1995.